Journal of Solid State Chemistry 281 (2020) 121044

Contents lists available at ScienceDirect

Journal of Solid State Chemistry

journal homepage: www.elsevier.com/locate/jssc

Effect of pH in the hydrothermal preparation of monoclinic tungsten oxide

Teodóra Nagyné-Kovács [a,*], István Endre Lukács [b], Anna Szabó [c], Klara Hernadi [c], Tamás Igricz [d], Krisztina László [e], Imre M. Szilágyi [a], György Pokol [a,f]

[a] Department of Inorganic and Analytical Chemistry, Budapest University of Technology and Economics, Műegyetem rakpart 3, Budapest, H-1111, Hungary
[b] Research Institute for Technical Physics and Materials Science, Hungarian Academy of Sciences, Konkoly Thege M. út 29-33, Budapest, H-1121, Hungary
[c] Department of Applied and Environmental Chemistry, University of Szeged, Rerrich B.tér 1, Szeged, H-6720, Hungary
[d] Department of Organic Chemistry and Technology, Budapest University of Technology and Economics, Műegyetem rakpart 3, Budapest, H-1111, Hungary
[e] Department of Physical Chemistry and Materials Science, Budapest University of Technology and Economics, Műegyetem rakpart 3, Budapest, H-1111, Hungary
[f] Research Centre for Natural Sciences, Hungarian Academy of Sciences, Magyar tudósok körútja 2, Budapest, H-1117, Hungary

ARTICLE INFO

Keywords:
Monoclinic WO_3
Hydrothermal
pH
Morphology
Band gap

ABSTRACT

This paper presents the preparation of monoclinic WO_3 by a one-step hydrothermal method. The effect of very acidic pH (0.1) and the significance of various additives (CH_3COOH, $NaClO_4$, Na_2SO_4) were investigated. To clarify the role of pH on the obtained crystal structure and morphology, every synthesis using pH 1 were repeated, and the effect of temperature, using 180 and 200 °C, was also studied. All samples prepared at pH 0.1 were pure, well crystallized monoclinic WO_3 independently from the temperature, the presence and the quality of the additives. At 180 and 200 °C, applying CH_3COOH and $NaClO_4$ resulted nanosheets similar in size. With Na_2SO_4 additive at 180 °C sheets, at 200 °C sheets and also rods formed indicating that SO_4^{2-} was a capping agent only at 200 °C. For comparison, at pH 1 at both temperatures the crystalline phases and the morphologies varied depending on the type of the additive.

1. Introduction

Tungsten oxides are widely studied materials due to their versatile possibilities in everyday use. They can catalyse many reactions e.g. CO oxidation [1], isomerization of alkenes [2], dehydrogenation of alcohols [3], hydrodesulphurization and hydrocracking [4,5], epoxidation of cycloocta-1,5-diene [6], Knoevenagel condensation [7] but can be also used as gas sensors [8–13] or photoanodes in electrochemical cells [14–16]. Additionally, their potential in photocatalysis has attracted many researchers' interest, since due to their smaller band gap (2.5–2.8 eV) than TiO_2 they are able to absorb not only ultra violet but visible light as well [17–25].

For the preparation of WO_3 powders or thin films there are numerous ways such as sol-gel method [14,15,26,27], spray pyrolysis [28,29], annealing of various W precursors [10,30,31], evaporation techniques [32,33] or hydrothermal procedures [34–41]. Among these, the hydrothermal method offers not only simple apparatus and usage, but also well-crystallized nanostructures.

In most cases the one-step hydrothermal treatment results hexagonal (h-) or orthorhombic (o-) WO_3 phase, and for the preparation of monoclinic (m-) WO_3 there is always need for a post calcination step [21,42–47]. The implementation for one-step hydrothermal synthesis of m-WO_3 without any post calcination would be huge improvement, since it is the most examined phase of WO_3. So far, however, only some papers have reported about its one-step hydrothermal synthesis [48–52]. Although, in these works the authors studied the effect of various parameters such as temperature, time, pH in the acidic range or concentration of the acid, the role of pH is still not clear. Since these preparations were carried out always in the presence of some additive, it is not clarified, whether the additive itself, the additive together with the adjusted pH, or only the pH is responsible for the formation of m-WO_3.

In this report, we prepared m-WO_3 by one-step hydrothermal reaction without any calcination using 0.1 pH. Moreover, we investigated the effects of different additives such as CH_3COOH in the volume of 1.25/2.5/5 and 7.5 mL, as well as Na_2SO_4 and $NaClO_4$. To get a definite answer to the effect of pH we carried out syntheses also at pH 1 and also without any additive. For revealing the influence of temperature, we used 180 and 200 °C as well. We investigated the obtained crystalline phases and morphology of the samples by XRD and SEM, then the pure m-WO_3 products were further examined by FT-IR, Raman, UV–Vis spectroscopy,

* Corresponding author.
E-mail address: kovacs.teodora@mail.bme.hu (T. Nagyné-Kovács).

https://doi.org/10.1016/j.jssc.2019.121044
Received 18 July 2019; Received in revised form 7 September 2019; Accepted 31 October 2019
Available online 1 November 2019

TEM and EDX. Finally, their specific surface area and band gaps were also determined.

2. Experimental

2.1. Hydrothermal synthesis

Every synthesis was carried out as the following: first, 4.1 g $Na_2WO_4{\cdot}H_2O$ was dissolved in 100 mL ion exchanged water. Under continuous stirring 3 M HCl acid solution was used to set the required pH. Next, 3.2 g $(COOH)_2{\cdot}2H_2O$ was added and the solution was completed up to 250 mL. In our former work we studied the role of oxalic acid and found, it improved the crystallinity of the products without changing the crystalline phases [53]. Based on this result, we used it in every preparation. In the following step, 30 mL solution was taken out and mixed with certain additive. Then, it was poured into a 45 mL autoclave (Parr Instruments) and put into a furnace at 180 or 200 °C for 24 h. Finally, the product was filtered, washed with ion exchanged water followed by ethanol and dried at 60 °C for 2 h.

The performed reactions are listed in Table 1. The obtained minor crystal phases are written in italics.

2.2. Characterization

For X-ray powder diffraction (XRD) measurements a PANanalytical X'Pert Pro MPD diffractometer with Cu Kα radiation (λ = 0.15418 nm), while for investigating the morphology of the samples a LEO 1540 XB electron microscope was used. Energy-dispersive X-ray spectroscopy (EDX) analyses were carried out by a JEOL JSM 5500-LV instrument. FT-IR spectra were taken by a PerkinElmer 2000 FT-IR spectrometer between 450 and 4000 cm^{-1} applying KBr pellets (1 mg sample/300 mg KBr). Raman spectra were recorded by a Jobin Yvon LabRam spectrometer equipped with an Olympus BX41 optical microscope using a frequency doubled Nd-YAG laser (532 nm), while diffuse reflectance UV–Vis spectra by a Jasco V-570 UV/VIS/NIR spectrometer. Transmission electron microscopy (TEM) images were taken by a FEI Tecnai G2 20 X-TWIN instrument operated at 200 keV. N_2 adsorption was measured at – 196 °C with a Nova2000e (Quantachrome) computer-controlled apparatus. The apparent surface area (S_{BET}) was calculated from the Brunauer–Emmett–Teller (BET) model [55].

3. Results and discussion

3.1. Crystal structure and morphology

3.1.1. Samples obtained at 180 °C, pH 0.1

Based on XRD patterns, samples **1**–**7** are identified as pure m-WO_3 (ICDD 04-005-4272) independently on the used additive (Fig. 1). The samples are well crystallized indicated by the sharp and narrow peaks without any other phases or impurities. In the case of using CH_3COOH a slight difference in crystallinity can be observed, i.e. the smaller acid volume improves it more, which is demonstrated by the much sharper reflections of samples **1** and **2**.

Based on the SEM images, not only the crystalline phase is the same, but also the morphology of samples **1–7** is very similar. Uniformly, the morphology consists of mostly sheets with cuboid-like shapes. In the case of using CH_3COOH additive, the sheets are generally 20–100 nm thick and 200–300 nm wide and long, and the ratio of the cuboids is getting more significant due to the larger volume of the acid (samples **1**–**4**, Fig. 2). The sample prepared with $NaClO_4$ has similar morphology, containing bit thicker, 50–200 nm sheets (samples **5**–**6**, Fig. 2), while using Na_2SO_4 additive results much more robust appearance of sheets, namely 100–200 nm thickness, 200–300 nm width and 350–800 nm length. Intriguingly, without additive, the morphology has the similar characteristics as sample **1** (sample **7**, Fig. 2).

Table 1
Experimental conditions of the performed hydrothermal reactions.

Sample	T (°C)	pH	Amount of additive	Crystalline phase	Morphology
1	180	0.1	1.25 mL CH_3COOH	m-WO_3	nanosheets
2	180	0.1	2.5 mL CH_3COOH		
3	180	0.1	5 mL CH_3COOH		
4	180	0.1	7.5 mL CH_3COOH		
5	180	0.1	2 g $NaClO_4$		
6	180	0.1	2 g Na_2SO_4		
7	180	0.1	–		
8	180	1.0	1.25 mL CH_3COOH	$WO_3{\cdot}0.33H_2O$	angular nanostructures
9	180	1.0	2.5 mL CH_3COOH		
10	180	1.0	5 mL CH_3COOH		
11	180	1.0	7.5 mL CH_3COOH		
* [54]	180	1.0	2 g $NaClO_4$		
* [53, 54]	180	1.0	2 g Na_2SO_4	h-WO_3	nanorods
* [53]	180	1.0	–	$WO_3{\cdot}0.33H_2O$	nanograins
12	200	0.1	1.25 mL CH_3COOH	m-WO_3	nanosheets
13	200	0.1	2.5 mL CH_3COOH		
14	200	0.1	5 mL CH_3COOH		
15	200	0.1	7.5 mL CH_3COOH		
16	200	0.1	2 g $NaClO_4$		
17	200	0.1	2 g Na_2SO_4		
18	200	0.1	–		
19	200	1.0	1.25 mL CH_3COOH	$WO_3{\cdot}0.33H_2O$, *m-WO_3*	angular nanostructures
20	200	1.0	2.5 mL CH_3COOH		
21	200	1.0	5 mL CH_3COOH		
22	200	1.0	7.5 mL CH_3COOH		
* [54]	200	1.0	2 g $NaClO_4$	$WO_3{\cdot}0.33H_2O$	angular nanostructures
* [53, 54]	200	1.0	2 g Na_2SO_4	h-WO_3	nanorods
	200	1.0	–	$WO_3{\cdot}0.33H_2O$	nanorods, nanograins

The asterisk at the samples prepared at pH 1 with the usage of $NaClO_4$, Na_2SO_4 or without additive refers to samples which we prepared in one of our former studies [53,54]. Thus, these results are not here reported in detail along with the last sample in Table 1 (200 °C, pH 1, without additive).

3.1.2. Samples obtained at 180 °C, pH 1

All XRD reflections are assigned to orthorhombic $WO_3{\cdot}0.33H_2O$ (ICDD 01-087-1203) in the case of using CH_3COOH additive (samples **8**–**11**, Fig. 3). The sharp, well distinguished peaks prove high degree of crystallinity of every sample independently from the volume of the acid.

On the SEM images homogenous morphology can be seen containing strongly agglomerated forms (Fig. 4). The $WO_3{\cdot}0.33H_2O$ crystals formed in angular shapes with 100–200 nm thickness and width and 200–300 nm length in the case of 1.25–5 mL CH_3COOH (samples **8–10**, Fig. 4). These become longer when 7.5 mL acid was used, in general, more than 300 nm (sample **11**, Fig. 4).

3.1.3. Samples obtained at 200 °C, pH 0.1

Every sample is identified as pure, single phase m-WO_3 with high crystallinity (Fig. 5). The lower volume of CH_3COOH is more beneficial as it gives narrower and sharper XRD peaks. Similar was observed in the case of 180 °C.

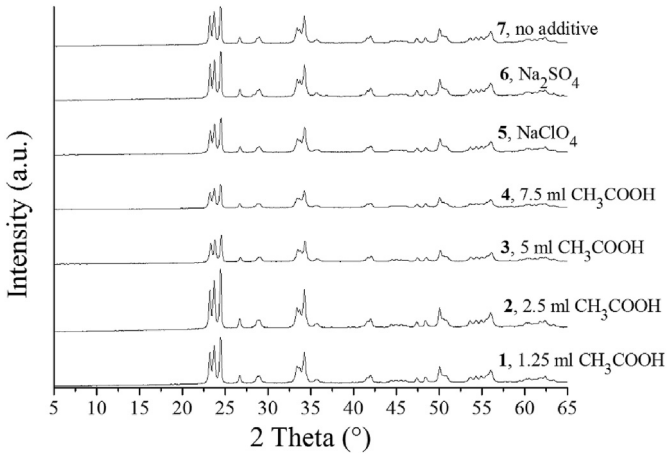

Fig. 1. XRD patterns of samples **1**–**7** (180 °C, pH 0.1).

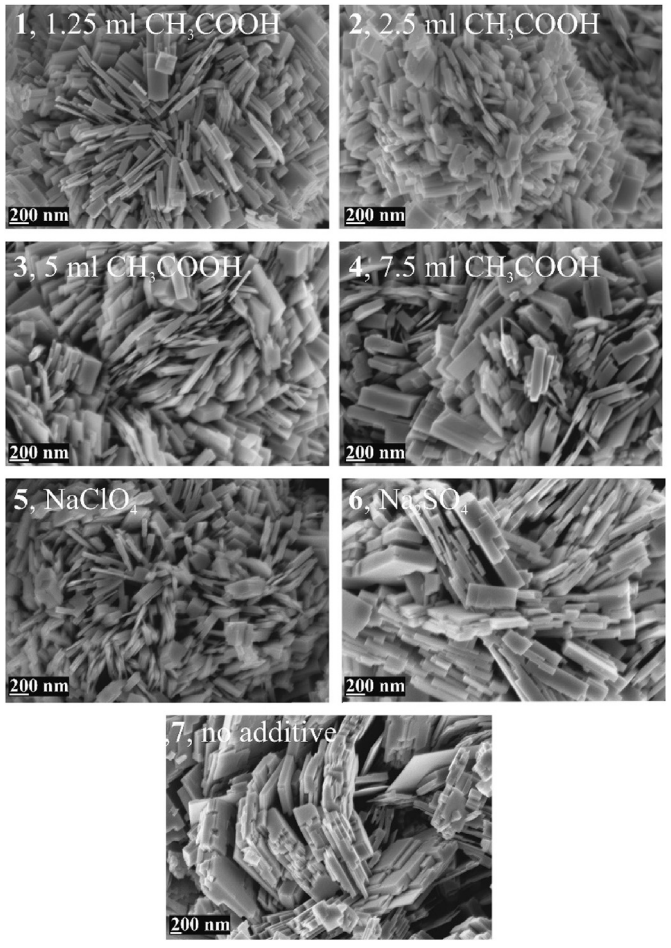

Fig. 2. SEM images of samples **1**–**7** (180 °C, pH 0.1).

Fig. 6 shows the homogenous, well defined morphology of samples **12**–**18**. Nanosheets are the characteristic forms when CH_3COOH or $NaClO_4$ and even when no additive were used, however, elongated, anisotropic forms appear when Na_2SO_4 was applied. The sheets are 20–100 nm thick and 200–300 nm wide in the case of CH_3COOH, similarly to those observed at 180 °C, but became much longer from 300 to 800 nm due to the higher temperature. Beside the thin sheets, cubes and wider angular forms also appear in some places (samples **12**–**15**, Fig. 6). When $NaClO_4$ was used, 100–200 nm thick and 200–300 nm width

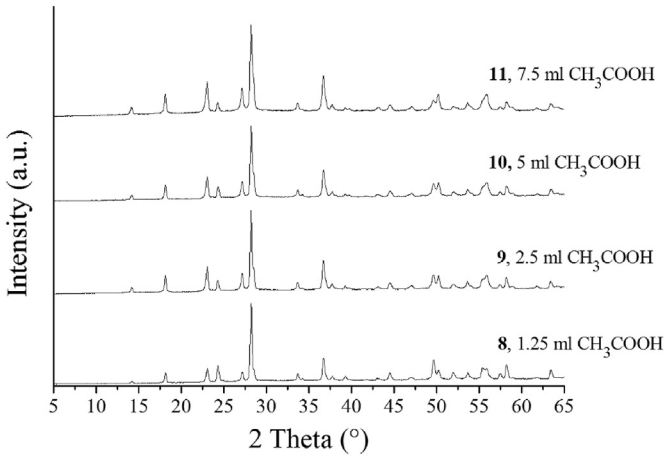

Fig. 3. XRD patterns of samples **8**–**11** (180 °C, pH 1).

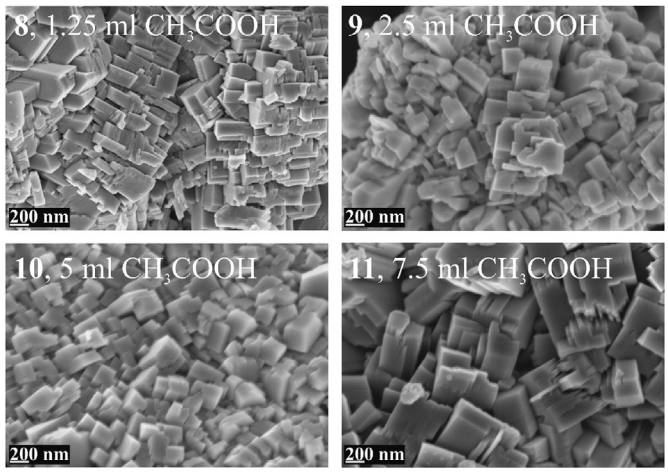

Fig. 4. SEM images of samples **8**–**11** (180 °C, pH 1).

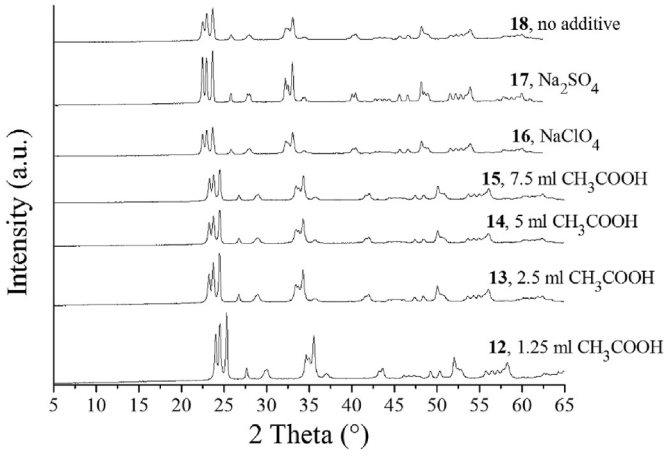

Fig. 5. XRD patterns of samples **12**–**18** (200 °C, pH 0.1).

sheets formed with more than 400 nm length (sample **16**, Fig. 6). When no additive was used, the obtained morphology was similar to samples **12**–**16** (sample **18**, Fig. 6). In the case of Na_2SO_4 additive, however, the morphology is mainly consisted of rods along with the sheets and consisted of mainly rods along with sheets. These rods are 200–400 nm thick and wide and can be even more than 1 μm long.

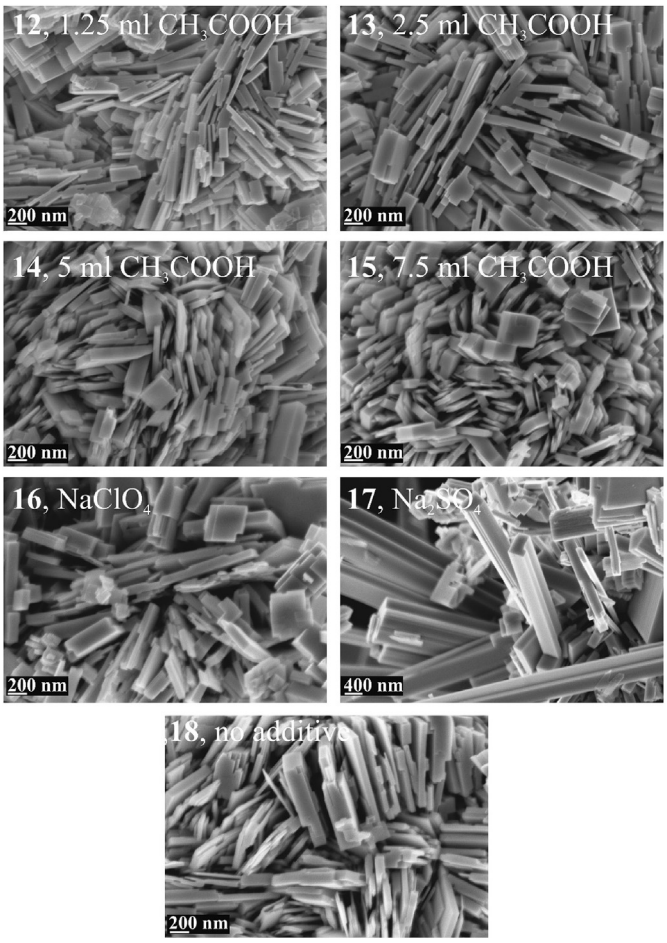

Fig. 6. SEM images of samples **12**–**18** (200 °C, pH 0.1).

The effect of Na_2SO_4 additive on the crystalline phase and morphology in the hydrothermal reaction of Na_2WO_4 and HCl is well known. It results hexagonal (h-)WO_3 with rod-like morphology at around pH 1 [53,56,57]. Its role as a capping agent in this work, however, seemed to be varying. Based on the XRD and SEM results neither h-WO_3, nor rods formed at pH 0.1, 180 °C (Figs. 1–2). At 200 °C, however, the effect of Na_2SO_4 additive on the morphology can be observed and the product contained rod-like figures as well beside nanosheets.

3.1.4. Samples obtained at 200 °C, pH 1

Samples **19**–**22** were identified as crystalline $WO_3{\cdot}0.33H_2O$ with small amount of m-WO_3 (Fig. 7). The ratio of m-WO_3 phase decreases along with the decreasing volume of CH_3COOH.

Samples **19**–**22** have similar morphology consisting of objects with shorter and longer angular shapes (Fig. 8). They are, in general, at least 200 nm thick, 200–300 nm wide and 200–800 nm long. Comparing them to samples **8**–**11**, prepared at 180 °C, we can conclude, that higher temperature is favourable for the growth of larger crystals. Due to that much greater but fewer crystal formed.

From the above detailed results we concluded, that neither the quality of the additive, nor the temperature had considerable influence on the obtained crystalline phase at pH 0.1. The formation of the m-WO_3 phase can be attributed only to the highly acidic pH. Therefore, we further investigated only the as-prepared new m-WO_3 phase found in samples **1**–**7**.

3.2. Elemental composition (EDX)

A typical EDX spectrum shows the main components of samples **1**–**7**, namely W and O (Fig. 9A). There are no other elements present referring to any impurity.

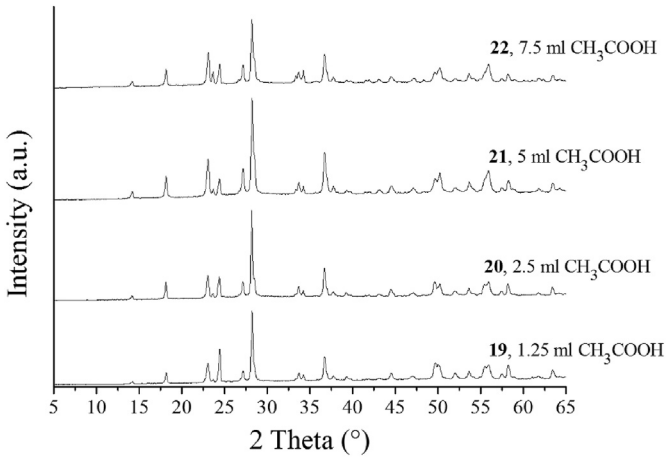

Fig. 7. XRD patterns of samples **19**–**22** (200 °C, pH 1).

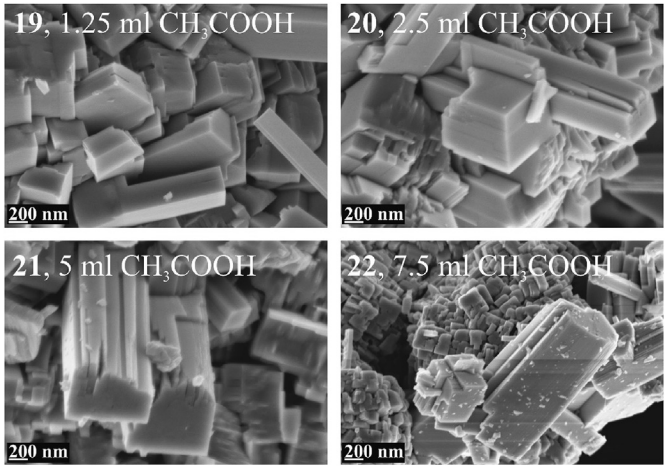

Fig. 8. SEM images of samples **19**–**22** (200 °C, pH 1).

3.3. FT-IR, Raman spectroscopy

In the FT-IR spectra of samples **1**–**7**, the region of 1000 and 500 cm^{-1} refers to the characteristic lattice vibrations of WO_3 (Fig. 9B). There are three well distinct peaks at around 750, 815 and 950 cm^{-1}, which belong to ν(W–O), ν(W–O–W) and ν(W–O, W═O), respectively. The broad peak at 3400-3600 cm^{-1} along with the band at 1600 cm^{-1} and in the case of some samples at 1400 cm^{-1} are ascribed to the vibration of ν_{sym} (OH) of hydroxyl group as well as δ(OH) and ν(OH) of W–OH interaction, respectively (framed in Fig. 9B) [11,58–61]. The appearance of the latter is more considerable when the volume of the acetic acid additive increases (samples **3**–**4**) and in the case of $NaClO_4$ additive (sample **5**).

Fig. 9C shows the Raman spectra of samples **1**–**7** which are the same without any difference in contrast with the FT-IR spectra. The main peaks at 810 and 710 cm^{-1} are ascribed to the stretching vibrations of m-WO_3. Bands appearing at 320 and 270 cm^{-1} are assigned to the bending modes, while the less intensive ones below 200 cm^{-1} belong to the lattice vibrations of the monoclinic phase [15,23,62–65].

3.4. UV–Vis spectroscopy, band gap

According to the diffuse reflectance UV–Vis spectra of samples **1**–**7**, significant absorption develops only in UV and the UV-near region of the

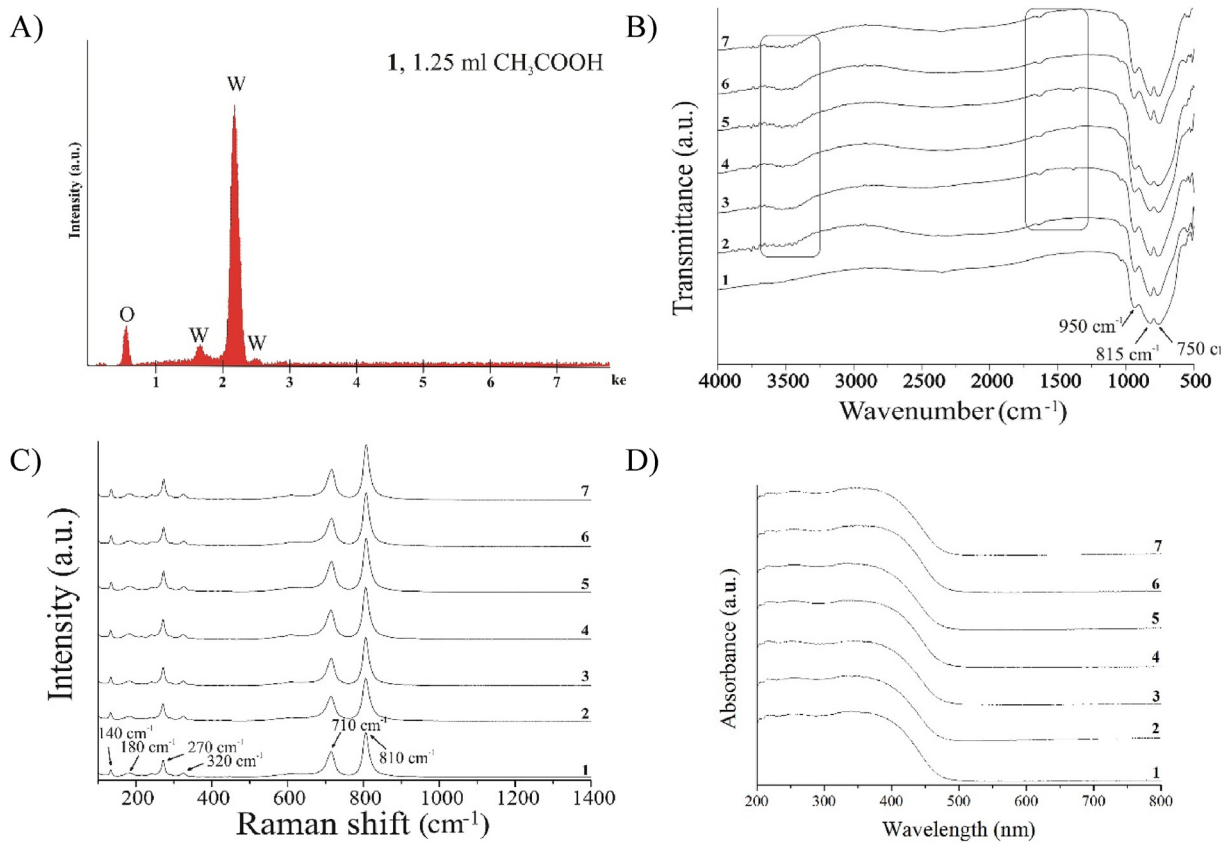

Fig. 9. A typical EDX spectrum (A), FT-IR (B), Raman (C) and diffuse reflectance UV–Vis spectra (D) of samples 1-7.

visible light (Fig. 9D). Their absorption edge is located at 450–460 nm in good agreement to the light yellow colour of m-WO_3 phase.

Based on the spectra, the band gaps were also calculated (Table 2). Calculation was carried out using $\alpha h\upsilon = A\ (h\upsilon - E_g)^n$ equation, where α is molar absorption coefficient, $h\upsilon$ is the photon energy, A is a constant, E_g is the band gap energy and n is depending on the direct or indirect allowed or forbidden type of the electron transition of the material, but is 2 for WO_3. With plotting $\alpha h\upsilon$ against $h\upsilon$ (Tauc-plot), drawing a tangent line onto the linear range and extrapolating, the value at $h\upsilon = 0$ gave the band gap energy (eV). For approximating A, Kubelka-Munk function was used [51,66–68]. Table 2 shows the band gap energy of each sample derived from diffuse reflectance spectra which are in good accordance with the reported range (2.5–3.0) [17,21,22,51,69–71]. The calculated values are technically equal which means, that neither the quality, nor the quantity of the used additives change the optical properties of m-WO_3 phase.

3.5. TEM

The TEM images show, that the 150–250 nm wide sheets are single crystalline and have smooth surface (Fig. 10). Their strict, straight edges can be clearly seen confirming the angular shapes appeared on the SEM images. Their thinness agrees with the SEM images and is obvious due to the visibility of other sheets ordered under each other. This up and down ordering is confirmed by the step-like edges at samples **5** and **6**.

Table 2
Calculated band gap of samples **1**–**7**.

	1	2	2	4	5	6	7
E_g, Band gap (eV)	2.58	2.57	2.57	2.57	2.58	2.58	2.57

For further investigating the nanosheet morphology of m-WO_3, TEM images were also taken of samples **1**, **5** and **6**, and their specific surface area were also determined.

3.6. Specific surface area

The apparent surface area of the samples is listed in Table 3. S_{BET} of samples **1** and **5** are comparable, considering the similar nanosheet morphology, however, **6** has much smaller area which can be attributed to the more robust appearance of sheets, which were considerably thicker than in the case of samples **1** and **5**, as discussed in 3.1.1.

4. Conclusion

In this study, we successfully prepared m-WO_3 using pH in the very acidic range (pH 0.1) during a one-step hydrothermal method without any post-calcination. Besides, we investigated the effect of various additives such as CH_3COOH in different volumes (1.25/2.5/5.0/7.5 mL), as well as $NaClO_4$, Na_2SO_4 and changed the temperature from 180 to 200 °C. As reference we carried out reactions using no additive, as well. To find out the role of pH in the formation of m-WO_3 we repeated every synthesis at pH 1. The samples prepared at pH 0.1 at 180 °C and 200 °C were pure m-WO_3 in all cases, independently on the type or on the presence of the additive. The samples had similar, nanosheet-like morphology in the case of CH_3COOH, $NaClO_4$ and even when no additives were used, at 180 and also at 200 °C. When Na_2SO_4 was used, however, elongated sheets were obtained at 180 °C, but the morphology consisted of mainly rods with more than 1 μm length at 200 °C. The appearance of the elongated sheets and rods can be attributed to the structure directing role of Na_2SO_4. Applying pH 1, the usage of CH_3COOH in every volume, $NaClO_4$ and the absence of any additives resulted $WO_3{\cdot}0.33H_2O$, but Na_2SO_4 gave h-WO_3. The morphology was affected by the type of the additives. The m-WO_3 samples prepared at pH 0.1 were further studied by EDX, FT-IR, Raman and UV–Vis spectroscopies, TEM and their band gap (2.57 eV) and specific surface area were

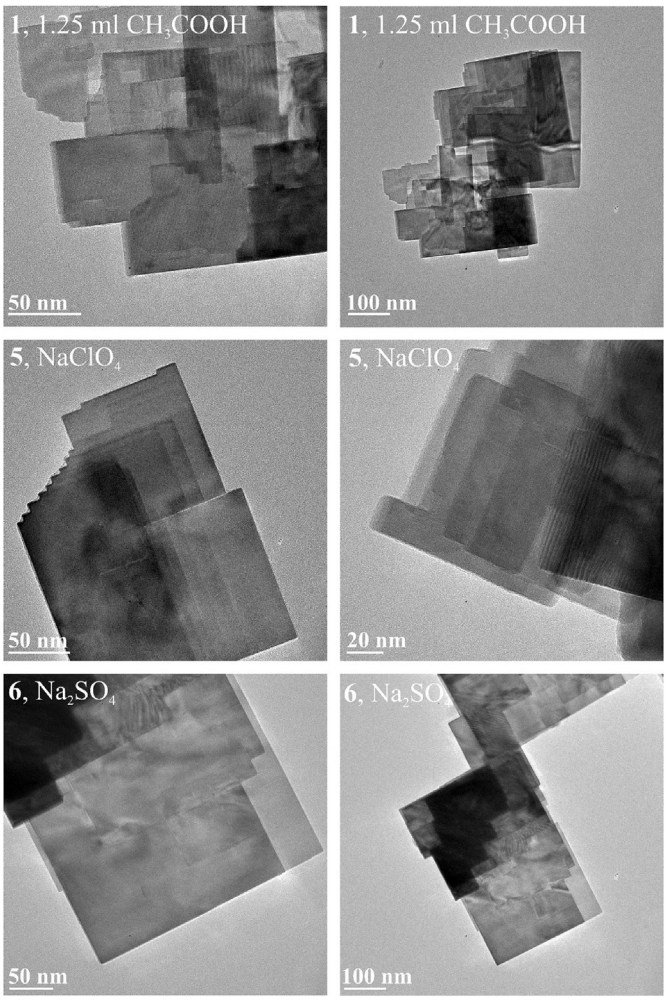

Fig. 10. TEM images of **1**, **5** and **6**.

Table 3
Specific surface area of samples **1**, **5** and **6**.

	1	5	6
S_{BET} (m [2]/g)	9.0	11	5.8

also determined.

Declarations of interest

none.

Acknowledgements

T. Nagyné-Kovács thanks for the József Varga Research Scholarship. I. M. Szilágyi thanks for a János Bolyai Research Fellowship of the Hungarian Academy of Sciences and for the ÚNKP-18-4-BME-238 New National Excellence Program of the Ministry of Human Capacities, Hungary. A GINOP-2.2.1-15-2017-00084, an NRDI K 124212 and an NRDI TNN_16 123631 grants are acknowledged. The work performed within project VEKOP-2.3.2-16-2017-00013 was supported by the European Union and the State of Hungary, co-financed by the European Regional Development Fund. The research reported in this paper was supported by the Higher Education Excellence Program of the Ministry of Human Capacities in the frame of Nanotechnology and Materials Science research area of Budapest University of Technology (BME FIKP-NAT).

References

[1] T. Firkala, et al., Influence of the support crystal structure of WO_3/Au catalysts in CO oxidation, Catal. Lett. 144 (2014) 831–836.
[2] R.D. Wilson, D.G. Barton, C.D. Baertsch, E. Iglesia, Reaction and deactivation pathways in xylene isomerization on zirconia modified by tungsten oxide, J. Catal. 194 (2000) 175–187.
[3] C.D. Baertsch, K.T. Komala, Y.-H. Chua, E. Iglesia, Genesis of brønsted acid sites during dehydration of 2-butanol on WO_3 catalysts, J. Catal. 205 (2002) 44–57.
[4] T. Kabe, W. Qian, A. Funato, Y. Okoshi, A. Ishihara, Hydrodesulfurization and hydrogenation on alumina-supported tungsten and nickel-promoted tungsten catalysts, Phys. Status Solidi A 1 (1999) 921–927.
[5] Y. Rezgui, M. Guemini, Effect of acidity and metal content on the activity and product selectivity for n -decane hydroisomerization and hydrocracking over nickel – tungsten supported on silica – alumina catalysts, Appl. Catal. A Gen. 282 (2005) 45–53.
[6] R. Gao, et al., High-activity, single-site mesoporous WO_3-MCF materials for the catalytic epoxidation of cycloocta-1,5-diene with aqueous hydrogen peroxide, J. Catal. 256 (2008) 259–267.
[7] D. Hunyadi, et al., WO3-EDA hybrid nanoplates and nanowires: synthesis, characterization, formation mechanism and thermal decomposition, RSC Adv. 7 (2017) 46726–46737.
[8] W. Zeng, et al., Hydrothermal synthesis, characterization of h-WO_3 nanowires and gas sensing of thin film sensor based on this powder, Thin Solid Films 584 (2015) 294–299.
[9] W. Yan, M. Hu, P. Zeng, S. Ma, M. Li, Room temperature NO_2-sensing properties of WO3 nanoparticles/porous silicon, Appl. Surf. Sci. 292 (2014) 551–555.
[10] I.M. Szilágyi, et al., Preparation of hexagonal WO_3 from hexagonal ammonium tungsten bronze for sensing NH3, Mater. Res. Bull. 44 (2009) 505–508.
[11] T. Nguyen, et al., Polycrystalline tungsten oxide nanofibers for gas-sensing applications, Sens. Actuators B Chem. 160 (2011) 549–554.
[12] I.M. Szilágyi, et al., Gas sensing selectivity of hexagonal and monoclinic WO_3 to H_2S, Solid State Sci. 12 (2010) 1857–1860.
[13] I.M. Szilágyi, et al., Controlling the composition of nanosize hexagonal WO_3 for gas sensing, Mater. Sci. Forum 589 (2008) 161–166.
[14] M. Yagi, S. Maruyama, K. Sone, K. Nagai, T. Norimatsu, Preparation and photoelectrocatalytic activity of a nano-structured WO_3 platelet film, J. Solid State Chem. 181 (2008) 175–182.
[15] C. Santato, M. Odziemkowski, M. Ulmann, J. Augustynski, Crystallographically oriented mesoporous WO_3 films: synthesis, characterization, and applications, J. Am. Chem. Soc. 123 (2001) 10639–10649.
[16] W.L. Kwong, H. Qiu, A. Nakaruk, P. Koshy, C.C. Sorrell, Photoelectrochemical properties of WO_3 thin films prepared by electrodeposition, Energy Procedia 34 (2013) 617–626.
[17] D.B. Hernandez-Uresti, D. Sánchez-Martínez, A. Martínez-De La Cruz, S. Sepúlveda-Guzmán, L.M. Torres-Martínez, Characterization and photocatalytic properties of hexagonal and monoclinic WO_3 prepared via microwave-assisted hydrothermal synthesis, Ceram. Int. 40 (2014) 4767–4775.
[18] Z.G. Zhao, M. Miyauchi, Nanoporous-walled tungsten oxide nanotubes as highly active visible-light-driven photocatalysts, Angew. Chem. Int. Ed. 47 (2008) 7051–7055.
[19] F.A. Ofori, F.A. Sheikh, R. Appiah-Ntiamoah, X. Yang, H. Kim, A simple method of electrospun tungsten trioxide nanofibers with enhanced visible-light photocatalytic activity, Nano-Micro Lett. 7 (2015) 291–297.
[20] X. Chen, et al., Ultrathin, single-crystal WO_3 nanosheets by two-dimensional oriented attachment toward enhanced photocatalystic reduction of CO_2 into hydrocarbon fuels under visible light, ACS Appl. Mater. Interfaces 4 (2012) 3372–3377.
[21] H. Zhang, et al., Template-free facile preparation of monoclinic WO_3 nanoplates and their high photocatalytic activities, Appl. Surf. Sci. 305 (2014) 274–280.
[22] S.B. Upadhyay, R.K. Mishra, P.P. Sahay, Structural and alcohol response characteristics of Sn-doped WO_3 nanosheets, Sens. Actuators B Chem. 193 (2014) 19–27.
[23] B. Ahmed, S. Kumar, A.K. Ojha, P. Donfack, A. Materny, Facile and controlled synthesis of aligned WO_3 nanorods and nanosheets as an efficient photocatalyst material, Spectrochim. Acta Part A Mol. Biomol. Spectrosc. 175 (2017) 250–261.
[24] Q.H. Li, L.M. Wang, D.Q. Chu, X.Z. Yang, Z.Y. Zhang, Cylindrical stacks and flower-like tungsten oxide microstructures: controllable synthesis and photocatalytic properties, Ceram. Int. 40 (2014) 4969–4973.
[25] I.M. Szilágyi, et al., Photocatalytic properties of WO_3/TiO_2 core/shell nanofibers prepared by electrospinning and atomic layer deposition, Chem. Vap. Depos. 19 (2013) 149–155.
[26] G. Leftheriotis, S. Papaefthimiou, P. Yianoulis, A. Siokou, D. Kefalas, Structural and electrochemical properties of opaque sol-gel deposited WO_3 layers, Appl. Surf. Sci. 218 (2003) 275–280.
[27] L. Meda, et al., Photo-electrochemical properties of nanostructured WO_3 prepared with different organic dispersing agents, Sol. Energy Mater. Sol. Cells 94 (2010) 788–796.
[28] M. Regragui, et al., Preparation and characterization of pyrolytic spray deposited electrochromic tungsten trioxide films, Thin Solid Films 358 (2000) 40–45.
[29] R. Sivakumar, et al., Preparation and characterization of spray deposited n-type WO_3 thin films for electrochromic devices, Mater. Res. Bull. 39 (2004) 1479–1489.
[30] G.R. Bamwenda, H. Arakawa, Visible light induced photocatalytic activity of tungsten trioxide powders, Appl. Catal. A Gen. 210 (2001) 181–191.
[31] I.M. Szilágyi, et al., Stability and controlled composition of hexagonal WO_3, Chem. Mater. 20 (2008) 4116–4125.

[32] R. Sivakumar, R. Gopalakrishnan, M. Jayachandran, C. Sanjeeviraja, Preparation and characterization of electron beam evaporated WO_3 thin films, Opt. Mater. 29 (2007) 679–687.
[33] D. Meng, T. Yamazaki, Y. Shen, Z. Liu, T. Kikuta, Preparation of WO_3 nanoparticles and application to NO_2 sensor, Appl. Surf. Sci. 256 (2009) 1050–1053.
[34] T. Peng, et al., Hexagonal phase WO_3 nanorods: hydrothermal preparation, formation mechanism and its photocatalytic O_2 production under visible-light irradiation, J. Solid State Chem. 194 (2012) 250–256.
[35] T. Kida, A. Nishiyama, M. Yuasa, K. Shimanoe, N. Yamazoe, Highly sensitive NO_2 sensors using lamellar-structured WO_3 particles prepared by an acidification method, Sens. Actuators B Chem. 135 (2009) 568–574.
[36] L. Zhou, et al., Green synthesis of hexagonal-shaped WO_3 $0.33H_2O$ nanodiscs composed of nanosheets, Cryst. Growth Des. 8 (2008) 3993–3998.
[37] Z. Gu, et al., Controllable assembly of WO_3 nanorods/nanowires into hierarchical nanostructures, J. Phys. Chem. B 110 (2006) 23829–23836.
[38] Z. Gu, et al., Large-scale synthesis of single-crystal hexagonal tungsten trioxide nanowires and electrochemical lithium intercalation into the nanocrystals, J. Solid State Chem. 180 (2007) 98–105.
[39] J. Huang, et al., Flower-like and hollow sphere-like WO_3 porous nanostructures: selective synthesis and their photocatalysis property, Mater. Res. Bull. 47 (2012) 3224–3232.
[40] F. Amano, M. Tian, G. Wu, B. Ohtani, A. Chen, Facile preparation of platelike tungsten oxide thin film electrodes with high photoelectrode activity, ACS Appl. Mater. Interfaces 3 (2011) 4047–4052.
[41] X. Feng, Y. Chen, Z. Qin, M. Wang, L. Guo, Facile fabrication of sandwich structured WO_3 nanoplate Arrays for efficient photoelectrochemical water splitting, ACS Appl. Mater. Interfaces 8 (2016) 18089–18096.
[42] A. Fujii, et al., Preparation of Pt-loaded WO_3 with different types of morphology and photocatalytic degradation of methylene blue, Surf. Coat. Technol. 271 (2015) 251–258.
[43] L. You, et al., Highly sensitive NO_2 sensor based on square-like tungsten oxide prepared with hydrothermal treatment, Sens. Actuators B Chem. 157 (2011) 401–407.
[44] J. Ram, et al., Effect of annealing on the surface morphology, optical and structural properties of nanodimensional tungsten oxide prepared by coprecipitation technique, J. Electron. Mater. 48 (2019) 1174–1183.
[45] S.J. Hong, H. Jun, P.H. Borse, J.S. Lee, Size effects of WO_3 nanocrystals for photooxidation of water in particulate suspension and photoelectrochemical film systems, Int. J. Hydrogen Energy 34 (2009) 3234–3242.
[46] S.S. Kalanur, Y.J. Hwang, S.Y. Chae, O.S. Joo, Facile growth of aligned WO_3 nanorods on FTO substrate for enhanced photoanodic water oxidation activity, J. Mater. Chem. 1 (2013) 3479–3488.
[47] Z. Liu, M. Miyauchi, T. Yamazaki, Y. Shen, Facile synthesis and NO_2 gas sensing of tungsten oxide nanorods assembled microspheres, Sens. Actuators B Chem. 140 (2009) 514–519.
[48] D. Jin, A. Phuruangrat, S. Thongtem, J. Sung, Hydrothermal synthesis of monoclinic WO_3 nanoplates and nanorods used as an electrocatalyst for hydrogen evolution reactions from water, Chem. Eng. J. 165 (2010) 365–369.
[49] J. Ma, et al., Topochemical preparation of WO_3 nanoplates through precursor H_2WO_4 and their gas-sensing performances, J. Phys. Chem. C 115 (2011) 18157–18163.
[50] S. Adhikari, D. Sarkar, Hydrothermal synthesis and electrochromism of WO_3 nanocuboids, RSC Adv. 4 (2014) 20145–20153.
[51] D. Nagy, D. Nagy, I.M. Szilagyi, X. Fan, Effect of the morphology and phases of WO_3 nanocrystals on their photocatalytic efficiency, RSC Adv. 6 (2016) 33743–33754.
[52] Y. Zhang, D. Zhang, X. Xu, B. Zhang, Morphology control and photocatalytic characterization of WO_3 nanofiber bundles, Chin. Chem. Lett. 29 (2018) 1350–1354.
[53] T. Nagyné-Kovács, et al., Preparation of iron tungstate ($FeWO_4$) nanosheets by hydrothermal method, Mater. Res. Bull. 95 (2017) 563–569.
[54] T. Nagyné-Kovács, et al., in: Effect of Different Anions upon the WO_3 Morphology and Structure, vol. 18, 2018, pp. 2–5.
[55] S. Brunauer, P.H. Emmett, E. Teller, Adsorption of gases in multimolecular layers, J. Am. Chem. Soc. 60 (1938) 309–319.
[56] Z. Gu, Y. Ma, W. Yang, G. Zhang, Yao, J. Self-assembly of highly oriented one-dimensional h-WO_3 nanostructures, Chem. Commun. 3597 (2005), https://doi.org/10.1039/b505429j.
[57] Y. Wu, Z. Xi, G. Zhang, J. Yu, D. Guo, Growth of hexagonal tungsten trioxide tubes, J. Cryst. Growth 292 (2006) 143–148.
[58] F.S. Manciu, J.L. Enriquez, W.G. Durrer, Y. Yun, Spectroscopic analysis of tungsten oxide thin films, J. Mater. Res. 25 (2010) 2401–2406.
[59] V.B. Kumar, D. Mohanta, Formation of nanoscale tungsten oxide structures and colouration characteristics, Bull. Mater. Res. 34 (2011) 435–442.
[60] N.Y. Bhosale, S.S. Mali, C.K. Hong, A.V. Kadam, Hydrothermal synthesis of WO_3 nanoflowers on etched ITO and their electrochromic properties, Electrochim. Acta 246 (2017) 1112–1120.
[61] V.I. Ethoxide, et al., Continuous flow synthesis of tungsten oxide (WO_3) nanoplates from tungsten (VI) ethoxide, Chem. Eng. J. (2013), https://doi.org/10.1016/j.cej.2013.03.094.
[62] M.F. Daniel, B. Desbat, J.C. Lassegues, B. Gerand, M. Figlarz, Infrared and Raman study of WO_3 tungsten trioxides and WO_3 xH_2O tungsten trioxide hydrates, J. Solid State Chem. 67 (1987) 235–247.
[63] A. Takase, K. Miyakawa, Raman study on sol-gel derived tungsten oxides from tungsten ethoxide, Jpn. J. Appl. Phys. 30 (1991) 1508–1511.
[64] I.M. Szilágyi, et al., WO_3 photocatalysts: influence of structure and composition, J. Catal. 294 (2012) 119–127.
[65] Z. Lu, M. Kanan, C.P. Tripp, Synthesis of high surface area monoclinic WO_3 particles using organic ligands and emulsion based methods, J. Mater. Chem. 12 (2002) 983–989.
[66] C.G. Granqvist, Electrochromic tungsten oxide: review of progress 1993-1998, Sol. Energy Mater. Sol. Cells 60 (2000) 201–262.
[67] R.S. Vemuri, M.H. Engelhard, C.V. Ramana, Correlation between surface chemistry, density, and band gap in nanocrystalline WO_3 thin films, ACS Appl. Mater. Interfaces 4 (2012) 1371–1377.
[68] K. Gesheva, A. Szekeres, T. Ivanova, in: Optical Properties of Chemical Vapor Deposited Thin Films of Molybdenum and Tungsten Based Metal Oxides, vol. 76, 2003, pp. 563–576.
[69] Sohail Azmat, S.Z. Ilyas Tariq Jan, Ather Hassan, Imtiaz Habib, A.M. Qasim Mahmood, Solar light triggered photocatalytic performance of WO_3 nanostructures; Waste water treatment, Mater. Res. Express 5 (2018) 115025.
[70] M. Oamar, et al., Selective photocatalytic oxidation of aromatic alcohols into aldehydes by tungsten blue oxide (TBO) anchored with Pt nanoparticles, RSC Adv. 6 (2016) 71108–71116.
[71] R.R. Kharade, S.R. Mane, R.M. Mane, P.S. Patil, P.N. Bhosale, Synthesis and characterization of chemically grown electrochromic tungsten oxide, J. Sol. Gel Sci. Technol. 56 (2010) 177–183.